J. Fluid Mech. (1991), *vol.* 233, *pp.* 369–388
Printed in Great Britain

Some characteristics of small-scale turbulence in a turbulent duct flow

By R. A. ANTONIA[1], J. KIM[2] AND L. W. B. BROWNE[1]

[1] Department of Mechanical Engineering, University of Newcastle, NSW 2308, Australia
[2] Center for Turbulence Research, NASA-Ames Research Center, Moffett Field, CA 94035, USA

(Received 13 December 1990 and in revised form 3 May 1991)

The fine-scale structure of turbulence in a fully developed turbulent duct flow is examined by considering the three-dimensional velocity derivative field obtained from direct numerical simulations at two relatively small Reynolds numbers. The magnitudes of all mean-square derivatives (normalized by wall variables) increase with the Reynolds number, the increase being largest at the wall. These magnitudes are not consistent with the assumption of local isotropy except perhaps near the duct centre-line. When the assumption of local isotropy is relaxed to one of local axisymmetry, or invariance with respect to rotation about a coordinate axis (here chosen in the streamwise direction), satisfactory agreement is indicated by the data outside the wall region. Support for axisymmetry is demonstrated by anisotropy invariant maps of the dissipation and vorticity tensors. The departure from axisymmetry does not appear to be affected by the Reynolds number. Expressions are proposed for approximations to the average energy dissipation and components of the mean-square vorticity. These proposals should allow these quantities to be measured accurately, at least in the present flow.

1. Introduction

Detailed information on the fine-scale structure of turbulence is required to provide accurate estimates of quantities such as the average turbulent energy dissipation and the mean-square vorticity. This information is needed in all flows, but more especially in the inner region of boundary-layer, duct and pipe flows. In particular, it can be used to enhance and improve turbulence models.

Measurements of nine of the twelve terms which appear in the expression for the average turbulent energy dissipation $\bar{\epsilon}$,

$$\bar{\epsilon} = \nu \overline{u_{i,j}(u_{i,j}+u_{j,i})} \tag{1}$$

(standard Cartesian tensor notation is used with $u_{i,j}$ representing the velocity derivative $\partial u_i/\partial x_j$; repeated indices imply summation), have been made in a self-preserving wake at a small value of the turbulence Reynolds number (Browne, Antonia & Shah 1987). These measurements also allowed most of the information for the mean-squared values of the three components of the vorticity vector $\omega_i = \epsilon_{ijk} u_{k,j}$ (ϵ_{ijk} is the alternating or unit permutation tensor, equal to $+1$ if i,j,k are in cyclic order, -1 if in anticyclic order, zero if any two of the i,j,k are equal) to be obtained (Antonia, Krishnamoorthy & Fulachier 1988).

The measurement of $u_{i,j}$ is much more difficult, primarily because of the spatial resolution requirement, in the near-wall region of boundary-layer, pipe or channel flows. Progress is, however, encouraging (e.g. the review by Foss & Wallace 1990 on

the measurement of vorticity) and simultaneous measurements of components of $u_{i,j}$ in a boundary layer have been reported (Balint, Vukoslavčević & Wallace 1990; Dracos *et al.* 1990) although not close to the wall and with relatively complex hot-wire configurations (a 9-hot-wire probe for Balint *et al.* and a 12-hot-wire probe for Dracos *et al.*). Direct numerical simulations (DNS) of turbulent wall shear flows (e.g. Kim, Moin & Moser 1987; Spalart 1988) provide complete three-dimensional information on the velocity field so that the velocity-derivative data bases generated by these simulations are especially suitable for exploring the statistics and structure of small-scale turbulence in the near-wall region. Use of these data bases has already been made to improve models, Reynolds stress and $k-\epsilon$, that can be applied all the way to the wall (Mansour, Kim & Moin 1988, 1989). In this paper, we use the data base for a fully developed turbulent duct flow to investigate in more detail the small-scale structure in this flow, and, in particular, the inter-relationship between the various components of $\bar{\epsilon}$ and those of the mean-square vorticity (sometimes fluctuating enstrophy)

$$\overline{\omega^2} \equiv \overline{\omega_i \omega_i} = \epsilon_{ijk}\epsilon_{imn}\overline{u_{k,j}u_{n,m}} \tag{2}$$

within a framework of concepts ranging between homogeneity and local isotropy (or isotropy of the small-scale motion).

Homogeneity, or invariance with respect to translation of the coordinate axes, permits a slight simplification to expressions (1), (2), namely

$$\bar{\epsilon}_{\text{hom}} = \nu\overline{u_{i,j}u_{i,j}}, \tag{3}$$

$$\overline{\omega^2_{\text{hom}}} = \bar{\epsilon}_{\text{hom}}/\nu. \tag{4}$$

Local isotropy – or invariance with respect to reflection and rotation about all coordinate axes – allows considerable simplification of (1) and (2), namely

$$\bar{\epsilon}_{\text{iso}} = 15\nu\overline{u^2_{1,1}}, \tag{5}$$

$$\overline{\omega^2_{\text{iso}}} = 15\overline{u^2_{1,1}}, \tag{6}$$

relation (5) having been first reported by Taylor (1935).

While the concept of local isotropy has received useful support from spectra of velocity derivatives at large wavenumbers (Antonia, Shah & Browne 1987), isotropic relations between mean-square values of velocity derivatives, and therefore (5) and (6), have not been satisfied by the available experimental data, irrespectively of the Reynolds number (e.g. Antonia, Anselmet & Browne 1986; Browne *et al.* 1987). Recently, Hussein (1988) and George & Hussein (1991, hereinafter referred to as I), showed, using their measurements in a relatively high-Reynolds-number round jet and those of Browne *et al.* (1987) in a low-Reynolds-number wake, that mean-square values of velocity derivatives are in quite reasonable agreement with local axisymmetry. The latter theory, which was introduced by Batchelor (1946) and extended by Chandrasekhar (1950), implies invariance with respect to rotation about a preferred direction. It therefore represents a considerable relaxation of the constraints imposed by local isotropy (spherical symmetry) although it is more constraining than homogeneity. Clearly, local axisymmetry and local isotropy share a common property: they both satisfy homogeneity. Conditions imposed by homogeneity on the velocity derivatives are satisfied by local axisymmetry and local isotropy. The agreement obtained in I between local axisymmetry (the streamwise direction was used as the preferred direction) and available measurements in free shear flows indicates that more accurate approximations can be obtained for quantities such as $\bar{\epsilon}$ and $\overline{\omega^2}$ than by invoking local isotropy. The implication of this

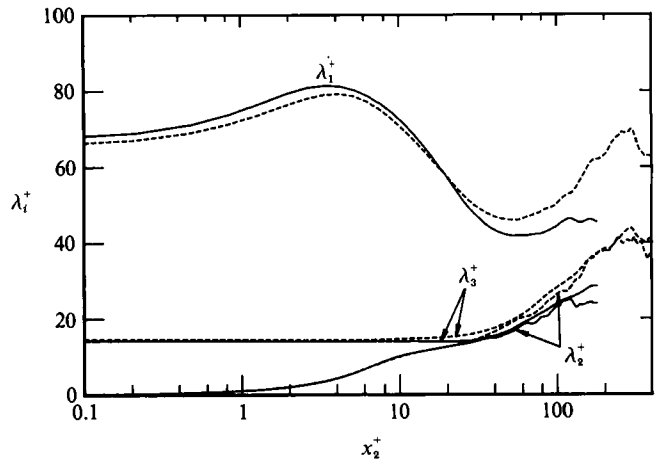

FIGURE 1. Taylor microscales in the x_1, x_2, x_3 directions. ——, $h^+ = 180$; – – – –, $h^+ = 395$.

result should be significant both experimentally and from a turbulence modelling perspective. Adequate testing of local axisymmetry (and local isotropy) requires that all velocity derivatives are available, thus making the DNS data bases indispensable for near-wall flows.

A note of caution should, however, be sounded with regard to the low Reynolds numbers (see §2 for details) of the present data bases. At such Reynolds numbers, the separation between the largest lengthscale (the channel width) and the smallest lengthscale (the Kolmogorov scale which is comparable to the viscous lengthscale in the wall region) is small. Consequently, the dissipation and energy-containing ranges of the spectrum are not independent and an inertial subrange does not exist.

2. DNS details and flow conditions

Direct numerical simulations (DNS) of fully developed duct flow were performed at $R = 3300$ and 7900, where R is a Reynolds number based on the centreline velocity and the channel half-width h. These latter values correspond to $h^+ (\equiv hU_\tau/\nu)$ values of about 180 and 395 respectively. The superscript + denotes normalization by the kinematic viscosity of the fluid ν and/or the friction velocity U_τ (unless otherwise stated, this normalization is used in all the figures). The numerical algorithm used and other details of the simulations can be found in Kim *et al.* (1987). For the $R = 3300$ case, $128 \times 129 \times 128$ spectral modes – in the x_1 (streamwise), x_2 (normal to the wall), x_3 (spanwise) directions respectively – were used in the computation. The spacings between collocation points in the streamwise and spanwise directions were $\Delta x_1^+ \approx 11$ and $\Delta x_3^+ \approx 4$. Non-uniform meshes were used in the normal direction, with the minimum spacing $\Delta x_2^+ \approx 0.05$ at the wall and the maximum spacing $\Delta x_2^+ \approx 4.4$ at the centreline. For $R = 7900$, roughly the same collocation grid spacings were used ($\Delta x_1^+ \approx 7, \Delta x_3^+ \approx 4, \Delta x_2^+ \approx 0.05$–$5.5$) to minimize the effect of grid resolution.

The flow is homogeneous in the x_1 and x_3 directions since, at any value of x_2, the averaging was carried out in both these directions. All the results presented in this paper were obtained by averaging over one field (one realization of 128×128 points in the (x_1, x_3)-plane) only. Several derivative statistics were computed by averaging over six fields, however, and no significant difference was observed, indicating that the samples used in the present study were adequate.

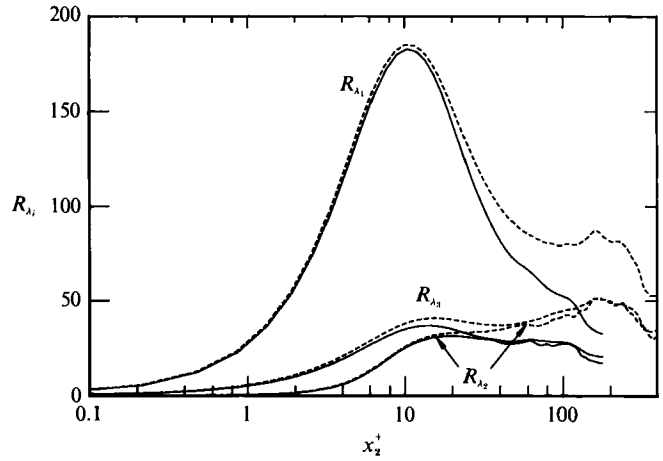

FIGURE 2. Turbulence Reynolds numbers. ——, $h^+ = 180$; – – – –, $h^+ = 395$.

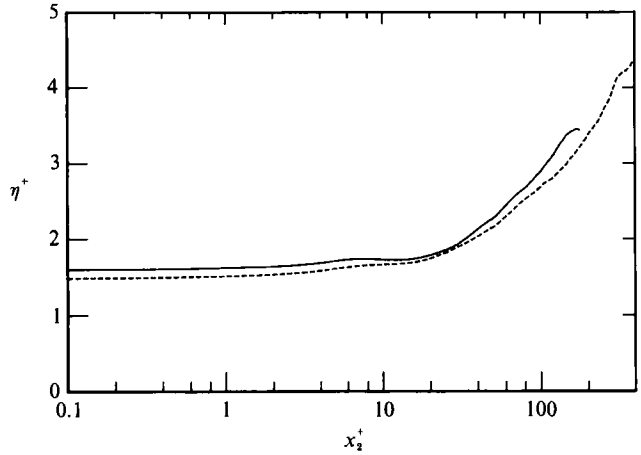

FIGURE 3. Kolmogorov microscale. ——, $h^+ = 180$; – – – –, $h^+ = 395$.

A detailed description of the flow conditions, including distributions of mean velocity, Reynolds stresses and higher-order moments of velocity fluctuations can be found in Kim *et al.* (1987) for $h^+ = 180$. For $h^+ = 395$, detailed statistics of pressure fluctuations were presented by Kim (1989) while distributions of the mean velocity and Reynolds stresses were given in Antonia *et al.* (1991). Information of relevance to the present study is presented in figures 1–3; a logarithmic scale is used for the abscissa, here and in subsequent figures, in order to emphasize the wall region. Figure 1 shows distributions of the Taylor microscales $\lambda_i^{+2} = \overline{u_1^{+2}}/\overline{u_{1,i}^{+2}}$. Close to the wall, λ_3^+ is approximately constant while λ_1^+ reaches a maximum near the edge of the viscous sublayer. There is essentially no Reynolds-number effect on λ_i^+ in he wall region. Outside the wall region, λ_2^+ and λ_3^+ are approximately equal and smaller than λ_1^+ by a factor of about 2.

The turbulent Reynolds numbers, defined by $R_{\lambda_i} = \overline{u_1^2}^{\frac{1}{2}} \lambda_i/\nu$, are given in figure 2. The largest value (≈ 180) is attained by R_{λ_1} at $y^+ \approx 10$. In the wall region, the magnitude of R_{λ_i} increases very slightly with h^+, the increase reflecting mainly the increase in $\overline{u_1^{+2}}^{\frac{1}{2}}$ with h^+. The Kolmogorov lengthscale $\eta = (\nu^3/\bar{\varepsilon})^{\frac{1}{4}}$ is plotted in figure 3. Like λ_3^+, η^+ is approximately constant in the wall region and increases in the outer region. Near $x_2^+ = 0$, η^+ is about 1.5, which is comfortably larger than the minimum

spacing of 0.05 used for Δx_2^+ in this region. Near the centre of the channel, the magnitude of Δx_2^+ (≈ 5) is comparable to η^+ and therefore adequate for resolving the smallest lengthscales. The resolution in the homogeneous x_1 and x_3 directions ($\Delta x_1^+ \approx 11$ and 7 and $\Delta x_3^+ \approx 4$) appears, at first sight, to be less adequate, especially very near the wall. Examination of computed spectra, however, showed no pile-up of energy at high wavenumbers even though the resolved grid scales in the horizontal directions were greater than the Kolmogorov lengthscale. In the wall region, it is less appropriate to compare Δx_1^+ and Δx_3^+ with η^+ since (see §3) the major contribution to $\bar{\epsilon}^+$ is from derivatives in the x_2 direction. The resolution Δx_2^+ ($= 0.05$) is quite adequate in this direction.

It is important to comment on the relatively small magnitudes of R_{λ_1} (figure 2). At the channel centreline, R_{λ_1} is about 30 at $h^+ = 180$ and 52 at $h^+ = 395$.

3. Distributions of $\bar{\epsilon}$, $\overline{\omega^2}$ and their components

In this section, we consider the distributions of $\bar{\epsilon}$ and $\overline{\omega^2}$ and of their components:

$$\bar{\epsilon} = \nu[2(\overline{u_{1,1}^2}+\overline{u_{2,2}^2}+\overline{u_{3,3}^2})+(\overline{u_{1,2}^2}+\overline{u_{2,1}^2}+\overline{u_{1,3}^2}+\overline{u_{3,1}^2}+\overline{u_{2,3}^2}+\overline{u_{3,2}^2}) + 2(\overline{u_{1,2}u_{2,1}}+\overline{u_{1,3}u_{3,1}}+\overline{u_{2,3}u_{3,2}})], \quad (7)$$

$$\overline{\omega^2} = \overline{u_{1,2}^2}+\overline{u_{2,1}^2}+\overline{u_{1,3}^2}+\overline{u_{3,1}^2}+\overline{u_{2,3}^2}+\overline{u_{3,2}^2}-2(\overline{u_{1,2}u_{2,1}}+\overline{u_{1,3}u_{3,1}}+\overline{u_{2,3}u_{3,2}}). \quad (8)$$

The nine square derivative terms which appear in (7) and (8) are plotted in figure 4. As expected, the major contributors near the wall are $\overline{u_{1,2}^2}$ and $\overline{u_{3,2}^2}$ (figure 4*a*; note that the vertical scale in figure 4(*b*, *c*) is greatly exaggerated by comparison to figure 4*a*). The contribution from $\overline{u_{1,3}^2}$ (figure 4*a*) becomes important outside the sublayer. It reaches a maximum near $x_2^+ = 15$ and is of the same order as $\overline{u_{1,2}^2}$ at larger values of x_2. There is a bump in the $\overline{u_{1,2}^2}$ distribution which corresponds approximately with the local maximum in $\overline{u_{1,3}^2}$. The bump in $\overline{u_{1,2}^2}$ and the peak in $\overline{u_{1,3}^2}$, both quite large in magnitude compared with $\overline{u_{1,1}^2}$ (figure 4*c*), may be due to the simultaneously large instantaneous gradients in $u_{1,2}$ and $u_{1,3}$ that are associated with low-speed streaks (e.g. Blackwelder & Swearingen 1990; Antonia & Bisset 1990). The relative shapes and relative magnitudes of the $\overline{u_{1,2}^2}$, $\overline{u_{1,3}^2}$ and $\overline{u_{1,1}^2}$ are very similar to those of $\overline{\theta_{,2}^2}$, $\overline{\theta_{,3}^2}$ and $\overline{\theta_{,1}^2}$ (θ is the temperature fluctuation) measured by Krishnamoorthy & Antonia (1987) in the wall region of a turbulent boundary layer. This similarity arises from the strong correlation in this region between u_1 and θ (e.g. Antonia, Browne & Shah 1988; Kim & Moin 1989).

Figure 4(*b*) shows the other three terms involving derivatives in either the x_2 or x_3 direction. All these terms have a maximum well away from the wall, the largest one being that of $\overline{u_{2,3}^2}$ (at $x_2^+ \approx 35$), one of the contributors to $\overline{\omega_1^2}$, the longitudinal mean-square vorticity. Terms involving derivatives in the x_1 direction (figure 4*c*) are generally smaller in magnitude than those in figure 4(*b* or *a*); $\overline{u_{1,1}^2}$ is the largest of the groups of terms in figure 4(*c*) in the wall region. The three cross-terms (not shown here) that appear in (7) and (8) have magnitudes comparable to the terms in figure 4(*c*), and make a negative contribution to $\bar{\epsilon}$ and a possible contribution to $\overline{\omega^2}$.

Except for $\overline{u_{1,3}^2}$, the magnitude of all terms in figure 4 increases as h^+ increases. This increase extends all the way to the wall, so that the Reynolds number affects the wall region as well as the outer region (the use of x_2^+ is inappropriate for this latter region; the Reynolds-number influence remained in evidence when the data were replotted in terms of x_2/h). At the wall, $\overline{u_{1,2}^2}$ and $\overline{u_{3,2}^2}$ increase by about 33%.

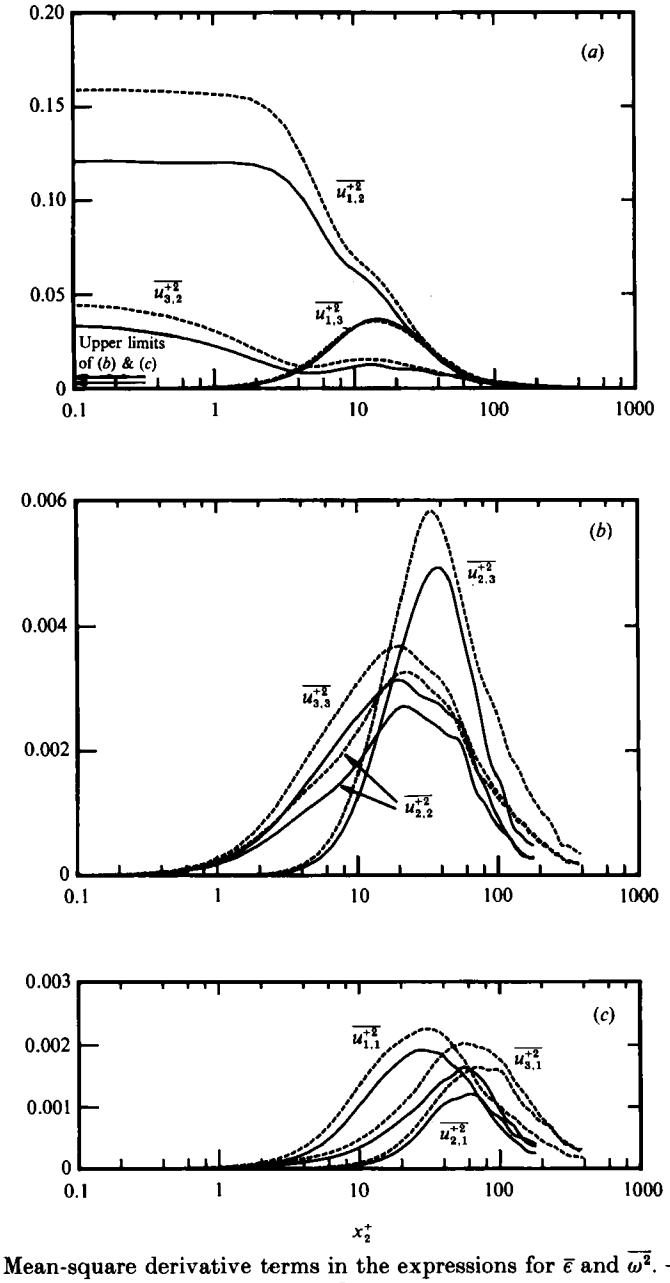

FIGURE 4. Mean-square derivative terms in the expressions for $\overline{\epsilon}$ and $\overline{\omega^2}$. ——, $h^+ = 180$; – – –, $h^+ = 395$.

The distributions of the three components of $\overline{\omega^2}$:

$$\overline{\omega_1^2} = \overline{u_{3,2}^2} + \overline{u_{2,3}^2} - 2\overline{u_{2,3}u_{3,2}}. \tag{9}$$

$$\overline{\omega_2^2} = \overline{u_{1,3}^2} + \overline{u_{3,1}^2} - 2\overline{u_{1,3}u_{3,1}}, \tag{10}$$

$$\overline{\omega_3^2} = \overline{u_{2,1}^2} + \overline{u_{1,2}^2} - 2\overline{u_{1,2}u_{2,1}}, \tag{11}$$

are shown in figure 5. These distributions are very similar to those in figure 4(*a*) (they

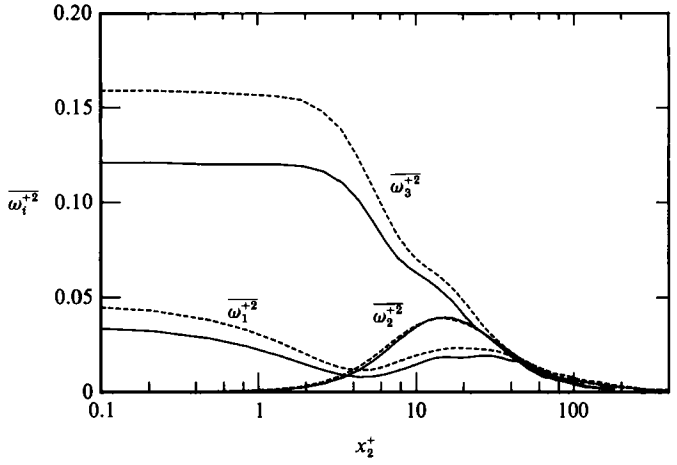

FIGURE 5. Distributions of the three components of mean-square vorticity. ——, $h^+ = 180$; – – –, $h^+ = 395$.

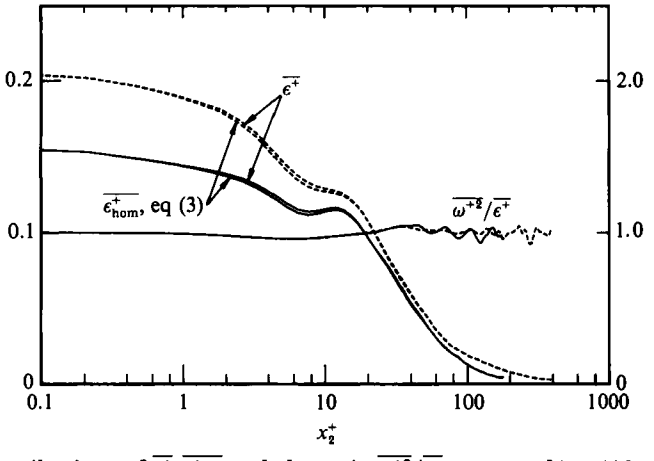

FIGURE 6. Distributions of $\overline{\epsilon^+}$, $\overline{\epsilon^+_{\rm hom}}$ and the ratio $\overline{\omega^{+2}}/\overline{\epsilon^+}$. ———, $h^+ = 180$; – –, $h^+ = 395$.

are identical at the wall) since the terms in figure 4(*a*) represent the dominant terms in $\overline{\omega_1^2}$, $\overline{\omega_2^2}$ and $\overline{\omega_3^2}$. The effect of Reynolds number on $\overline{\omega_1^2}$ and $\overline{\omega_3^2}$ is therefore considerable (an increase of about 33 % in each of these) but negligible on $\overline{\omega_2^2}$. The latter behaviour does not seem to be easily reconcilable with the notion of hairpin vortices being stretched with increasing Reynolds number since this would imply an increase in all three components; it is more consistent with a not necessarily connected agglomeration of longitudinal and spanwise vortices. The independence of $\overline{\omega_2^{+2}}$ of the Reynolds number is apparently consistent with the scaling of the average spanwise spacing (normalized by wall variables) of low-speed streaks.

Figure 6 shows that distributions of $\overline{\epsilon}^+$, equation (1), and $\overline{\epsilon}^+_{\rm hom}$, (3), are practically coincident, indicating that the net contribution of the cross-terms in $\overline{\epsilon}$ is negligible. The ratio $\overline{\epsilon}_{\rm hom}/\nu\overline{\omega^2_{\rm hom}}$ is also close to 1, consistent with (4), everywhere in the flow. Note that $\overline{\epsilon}$ is maximum at the wall but exhibits a local peak near $x_2^+ \approx 15$, where most of the quantities plotted in figure 4 exhibit a peak and the average turbulent energy production is a maximum (Kim *et al.* 1987).

4. Anisotropy invariant mapping

Lumley & Newman (1977) examined the anisotropy of the Reynolds stress tensor by considering the second (II) and third (III) invariants of b_{ij}, the Reynolds stress anisotropy tensor, defined by

$$b_{ij} = \frac{\overline{u_i u_j}}{2k} - \frac{\delta_{ij}}{3},$$

where $k \equiv \frac{1}{2}\overline{u_i u_i}$ is the average turbulent kinetic energy and δ_{ij} is the Kronecker delta tensor ($\delta_{ij} = 1$ for $i = j$ and 0 for $i \neq j$). The second and third invariants of b_{ij} are given by (the first invariant b_{ii} is zero for incompressible flows)

$$\mathrm{II} = -\tfrac{1}{2} b_{ij} b_{ji}, \tag{12}$$

$$\mathrm{III} = \tfrac{1}{3} b_{ij} b_{jk} b_{ki}. \tag{13}$$

All the states that characterize b_{ij} can be identified on a plot of $-\mathrm{II}$ *vs.* III. The limiting values of the invariants delineate an anisotropy invariant map (AIM) such as shown in figure 7. This plot has been used to examine, for example, the influence of boundary conditions (Dekeyser, Fulachier & Verollet 1977) and flow rotation (Reynolds 1989) on the anisotropy of the Reynolds stresses. DNS data permit AIMs to be constructed for other quantities such as dissipation and vorticity (Lee & Reynolds 1985; Mansour *et al.* 1988). In the case of dissipation, the anisotropy tensor is given by d_{ij}

$$d_{ij} = \frac{\bar{\epsilon}_{ij}}{2\bar{\epsilon}} - \frac{\delta_{ij}}{3},$$

where $\bar{\epsilon}_{ij} = 2\nu\overline{u_{i,k} u_{j,k}}$ and $\bar{\epsilon}$ is equal to half the scalar trace of $\bar{\epsilon}_{ij}$, namely $\bar{\epsilon} = \frac{1}{2}\bar{\epsilon}_{ii}$. For vorticity, the anisotropy tensor is denoted by v_{ij}:

$$v_{ij} = \frac{\overline{\omega_i \omega_j}}{\overline{\omega^2}} - \tfrac{1}{3}\delta_{ij}.$$

The second and third invariants of d_{ij} and v_{ij} are given by expressions analogous to (12) and (13).

The AIMs for b_{ij}, d_{ij} and v_{ij} are shown in figure 7 (*a–c*), respectively.

Very near the wall, the invariants reside near the upper boundary, which is described by $G \equiv \frac{1}{9} + 3\mathrm{III} + \mathrm{II} = 0$ and characterizes two-component turbulence (one component is zero). In the case of the Reynolds stress, $\overline{u_2^2}$ is negligible near the wall while one of the diagonal components ($\bar{\epsilon}_{22}$) of $\bar{\epsilon}_{ij}$ is negligible in this region. In the case of $\overline{\omega_i \omega_j}$, the component of vorticity normal to the wall is negligible near $x_2^+ = 0$. As x_2^+ increases, the upper boundary is followed in the direction of the top cusped vertex ($\mathrm{II} = \frac{8}{3}$, $\mathrm{III} = \frac{16}{9}$). This point corresponds to one-component turbulence (two components are zero). The invariants II and III reach a maximum before following the right-hand boundary of the AIM towards the bottom cusp ($\mathrm{II} = \mathrm{III} = 0$), which characterizes isotropic turbulence. The location of the maximum is at $x_2^+ \approx 8$ for the Reynolds stress, $x_2^+ \approx 4$ for the dissipation and $x_2^+ \approx 3$ for vorticity. The right-hand boundary of the AIM appears to be followed more closely by the dissipation and the vorticity than by the Reynolds stress data. The right- and left-hand boundaries of the AIM characterize axisymmetric turbulence. For example, in the case of v_{ij}, two of the components of $\overline{\omega_i \omega_j}$ are nearly equal while the third is larger (right-hand boundary) or smaller (left-hand boundary) than the other equal components.

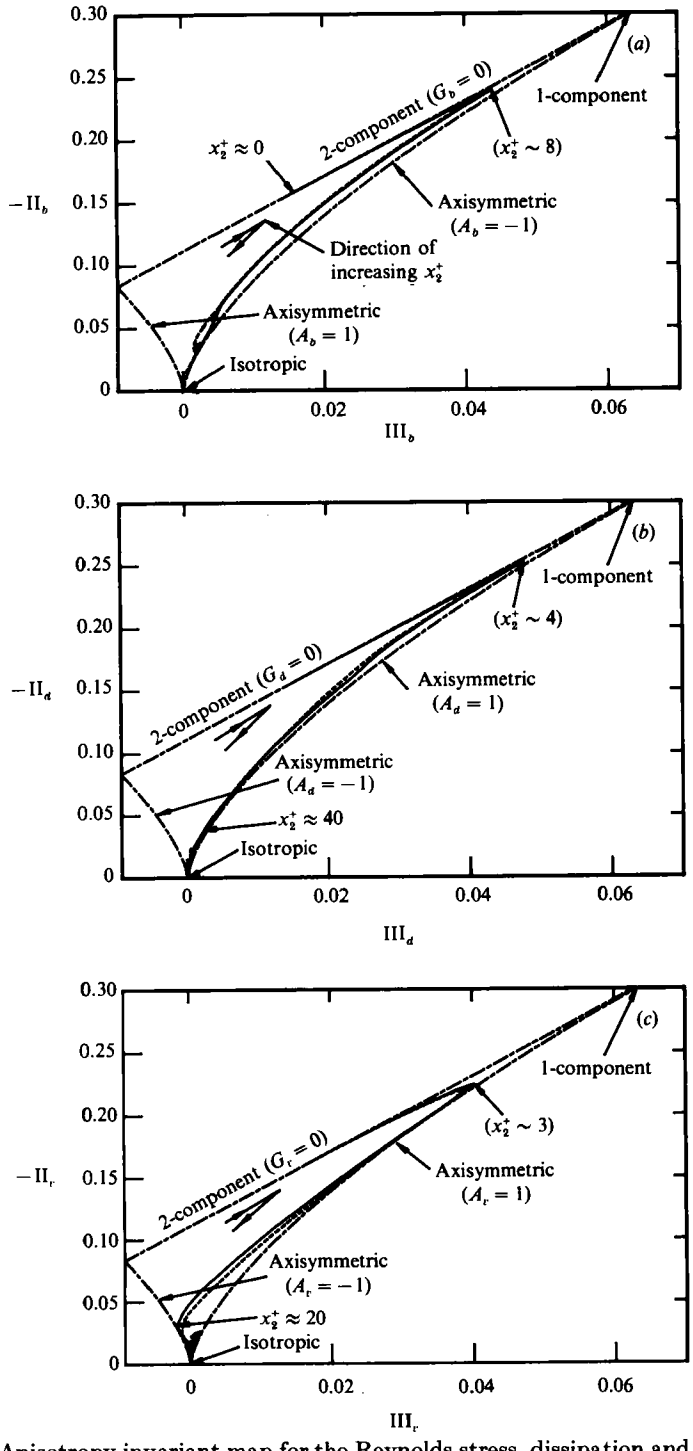

FIGURE 7. Anisotropy invariant map for the Reynolds stress, dissipation and vorticity tensors, the subscripts b, d and v indicating these tensors. (a) Reynolds stress; (b) dissipation; (c) vorticity. ——, $h^+ = 180$; – – –, $h^+ = 395$.

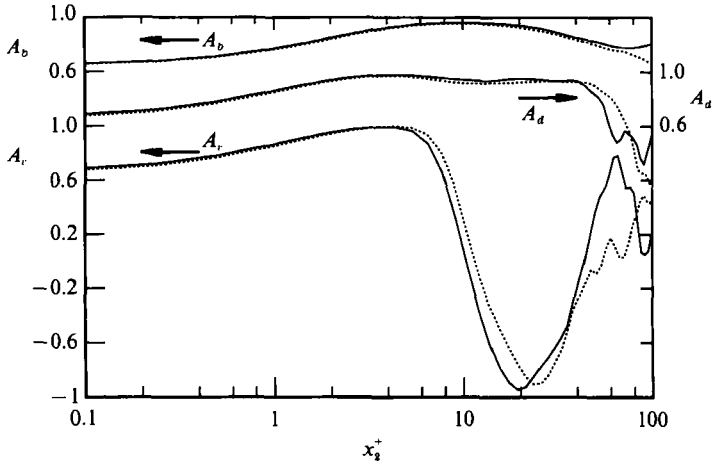

FIGURE 8. Measure of departure from local axisymmetry of Reynolds stress, dissipation and vorticity tensors. ——, $h^+ = 180$; – – –, $h^+ = 395$.

Lee & Reynolds (1985) described† this state as disk-like (the turbulence is pulled out in two directions and squeezed in the other direction) for the right-hand boundaries of the stress and dissipation AIMs and the left-hand boundary of the vorticity AIM. The left-hand boundary of the stress and dissipation AIMs and the right-hand boundary of the vorticity AIM were described as rod-like (turbulence consisting of elongated line vortices). These authors introduced a parameter A,

$$A = \frac{\frac{1}{2}\mathrm{III}}{(-\frac{1}{3}\mathrm{II})^{\frac{3}{2}}},$$

to illustrate the difference between the two modes of axisymmetric turbulence. A_b and A_d are equal to $+1$ for disk-like turbulence and -1 for rod-like turbulence. A_v is equal to 1 for rod-like turbulence and -1 for disk-like turbulence. The variation of A_b, A_d and A_v with x_2^+ is shown in figure 8. All three quantities approach $+1$ at the edge of the sublayer, with A_v actually reaching this value (see also figure 7*c*). A_d remains close to $+1$ throughout the wall region, decreasing somewhat abruptly for $x_2^+ \geqslant 40$. The magnitude of A_v changes rapidly from $+1$ to nearly -1 (at $x_2^+ \approx 20$) becoming positive again for larger values of x_2^+. The x_2^+ range in figure 8 has been restricted to $x_2^+ < 100$ as the behaviour of A_b, A_d and A_v becomes very erratic at larger x_2^+ (in this region, the magnitude of II becomes negligible). The behaviour of the vorticity AIM (figure 7*c*) and of A_v (figure 8) suggests a change from an elongated vortex structure at the edge of the sublayer to a disk-like structure near $x_2^+ \approx 20$. In this context, Townsend (1951) observed that conditions suitable for the production of vortex sheets are more common than for the production of vortex lines. By contrast, Kuo & Corrsin (1972) concluded that the fine structure of turbulence is more likely to be rod-like than either spherical or slab-shaped.

The information in figures 7 and 8, taken collectively, seems to support the existence of a rod-like structure near the edge of the sublayer and a change to a disk-like structure near $x_2^+ = 20$. While it is difficult to draw firm conclusions for larger x_2^+

† Reynolds (1989) emphasized however that, while b_{ij}, d_{ij} and v_{ij} contain information about 'componentality' (i.e. provide a measure of the relative importance of the stress, dissipation and vorticity components), they do not contain any information about the 'dimensionality' of turbulence.

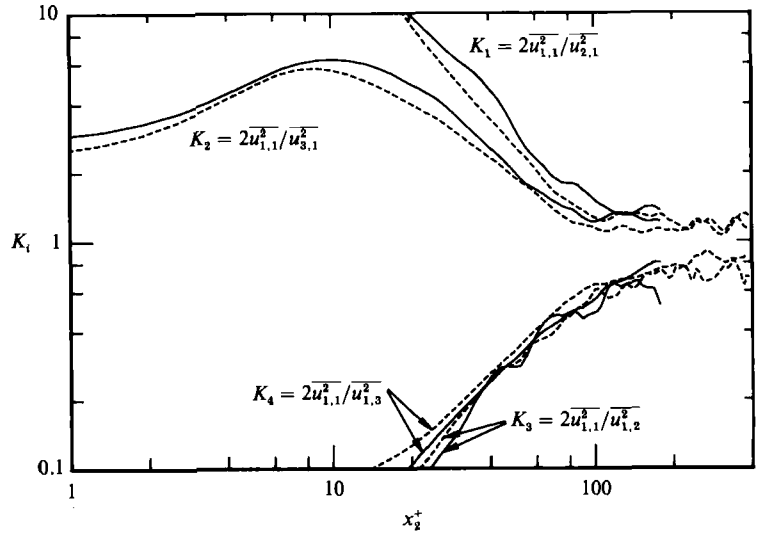

FIGURE 9. Distributions of $K_i, i = 1$ to 4, equation (14). ——, $h^+ = 180$; – – –, $h^+ = 395$.

on the basis of figure 8 (owing to the small magnitudes of the invariants in this region), the overall trend of the AIMs in figure 7 tends to favour a disk-like behaviour prior to approaching isotropy (near the channel centreline). Note that there is no discernible Reynolds-number effect on the turbulence states indicated by either the anisotropy invariant maps, figure 7, or the parameters A, figure 8.

Near the channel centreline, all three invariant maps in figure 7 indicate an approach towards isotropy, a trend which is also supported by the data in §5. Further, the high-wavenumber region of the spectra (not shown here) of all three velocity fluctuations agrees with local isotropy. Similar agreement has previously been noted (e.g. Champagne 1978) in high-turbulence-Reynolds-number flows but also in flows with values of R_{λ_1} comparable to the present centreline values.

5. Local axisymmetry *vs.* local isotropy

Local isotropy requires, *inter alia*, that the following ratios are all equal to 1:

$$K_1 \equiv 2\overline{u_{1,1}^2}/\overline{u_{2,1}^2} \quad K_2 \equiv 2\overline{u_{1,1}^2}/\overline{u_{3,1}^2}, \quad K_3 \equiv 2\overline{u_{1,1}^2}/\overline{u_{1,2}^2}, \quad K_4 \equiv 2\overline{u_{1,1}^2}/\overline{u_{1,3}^2}. \tag{14}$$

Browne *et al.*'s (1987) measurements in a turbulent wake and their review of available experimental data in a number of flows indicated that $K_1 \approx K_2 > 1$ while $K_3 \approx K_4 < 1$. The present distributions of K_i ($i = 1$ to 4), figure 9, are generally consistent with these trends, although K_1 is significantly larger than K_2 near the wall. These ratios approach 1 near the duct centreline. The effect of the Reynolds number is quite small, the magnitudes of K_i being slightly smaller at $h^+ = 395$ than $h^+ = 180$.

Local axisymmetry (with x_1 as the preferred axis) requires, *inter alia*, that the following ratios are equal to 1:

$$M_1 \equiv \overline{u_{1,2}^2}/\overline{u_{1,3}^2}, \quad M_2 \equiv \overline{u_{2,1}^2}/\overline{u_{3,1}^2}, \quad M_3 \equiv \overline{u_{2,2}^2}/\overline{u_{3,3}^2}, \quad M_4 \equiv \overline{u_{2,3}^2}/\overline{u_{3,2}^2}. \tag{15}$$

Equation (15) is, of course, a requirement for local isotropy also. $M_1 = 1$ implies that $K_3 = K_4$ while $M_2 = 1$ implies that $K_2 = K_1$. As noted above, the data examined by Browne *et al.* indicated reasonable support for $M_i = 1$, even though $K_i \neq 1$. The M_i

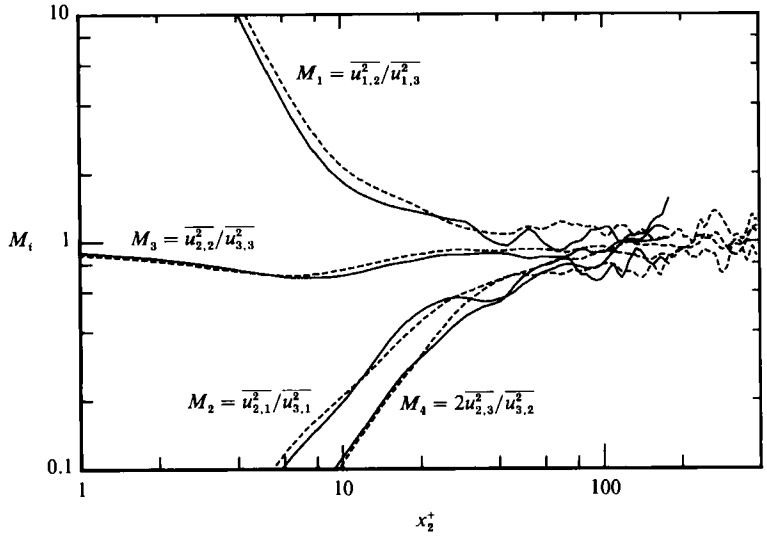

FIGURE 10. Distributions of $M_i, i = 1$ to 4, equation (15). ——, $h^+ = 180$; ---, $h^+ = 395$.

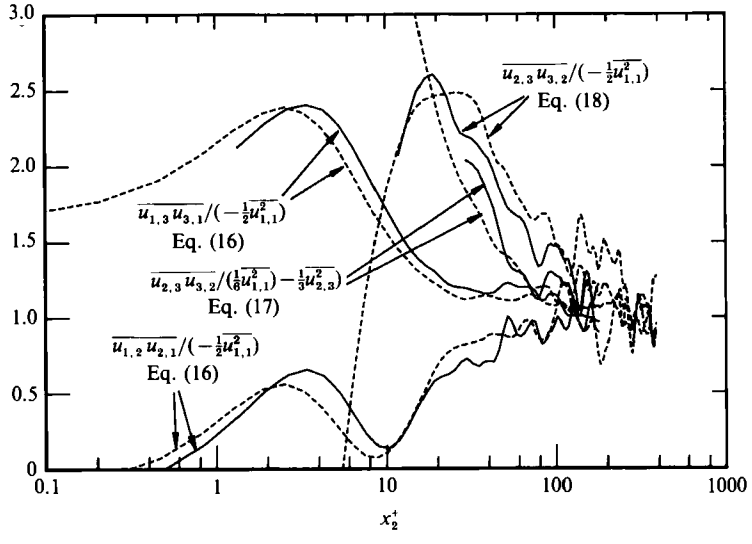

FIGURE 11. Comparison with axisymmetry and isotropy of cross-terms in (16), (17) and (18). ——, $h^+ = 180$; ---, $h^+ = 395$.

distributions in figure 10 approach 1 more rapidly than K_i. M_3 departs slightly from 1 near the edge of the sublayer. M_1 decreases as x_2^+ increases, reaching 1 in the region $x_2^+ \geqslant 40$. M_2 and M_4 increase towards 1, but the convergence is slower than for M_1.

Locally axisymmetric expressions for the three cross-terms that appear in relations (7) and (8) were given in I:

$$\overline{u_{1,2}u_{2,1}} = \overline{u_{1,3}u_{3,1}} = -\tfrac{1}{2}\overline{u_{1,1}^2}, \tag{16}$$

$$\overline{u_{2,3}u_{3,2}} = \tfrac{1}{6}\overline{u_{1,1}^2} - \tfrac{1}{3}\overline{u_{2,3}^2}. \tag{17}$$

Equation (16) also applies for local isotropy but the isotropic equivalent of (17) is

$$\overline{u_{2,3}u_{3,2}} = -\tfrac{1}{2}\overline{u_{1,1}^2} \tag{18}$$

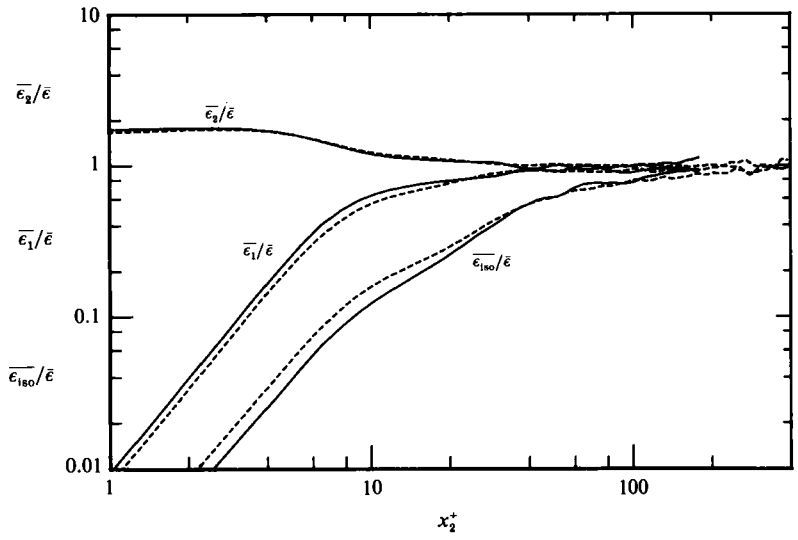

FIGURE 12. Axisymmetric and isotropic expressions for $\bar{\epsilon}$: $\overline{\epsilon_1}$, equation (19); $\overline{\epsilon_2}$, (20); $\overline{\epsilon_{iso}}$, (5). ——, $h^+ = 180$; – – –, $h^+ = 395$.

since all three cross-terms are equal. This follows from the isotropic requirement

$$\overline{u_{i,j}u_{k,m}}/(\tfrac{1}{2}\overline{u_{1,1}^2}) = 4\delta_{ik}\delta_{jm} - \delta_{ij}\delta_{km} - \delta_{im}\delta_{jk}.$$

The ratios of each of the cross-terms in (16)–(18) to $(-\frac{1}{2}\overline{u_{1,1}^2})$ are shown in figure 11. Also included in the figure is the ratio between the left- and right-hand sides of (17). Equation (16) is reasonably well satisfied for $x_2^+ \geqslant 50$ while (17) represents only a slight improvement over (18).

The assumption of local axisymmetry allows considerable simplification of relation (7) since only four terms are needed to estimate $\bar{\epsilon}$, as compared with the nine terms in the homogeneous relation (3). Two axisymmetric forms for $\bar{\epsilon}$ were written in I (with x_1 as the preferred axis), and are reproduced below as $\overline{\epsilon_1}$ and $\overline{\epsilon_2}$, namely

$$\overline{\epsilon_1} = \nu(\tfrac{5}{3}\overline{u_{1,1}^2} + 2\overline{u_{1,3}^2} + 2\overline{u_{2,1}^2} + \tfrac{8}{3}\overline{u_{2,3}^2}), \tag{19}$$

$$\overline{\epsilon_2} = \nu(-\overline{u_{1,1}^2} + 2\overline{u_{1,2}^2} + 2\overline{u_{2,1}^2} + 8\overline{u_{2,2}^2}). \tag{20}$$

Distributions of the ratios $\overline{\epsilon_1}/\bar{\epsilon}, \overline{\epsilon_2}/\bar{\epsilon}$ and $\overline{\epsilon_{iso}}/\bar{\epsilon}$ are shown in figure 12. While $\overline{\epsilon_{iso}}$ grossly underestimates $\bar{\epsilon}$ in the region $x_2^+ \leqslant 60$ (it is only half-$\bar{\epsilon}$ at $x_2^+ = 40$) and remains below it up to $x_2^+ \approx 120$, $\overline{\epsilon_1}$ and $\overline{\epsilon_2}$ are good approximations to $\bar{\epsilon}$ outside the buffer region ($x_2^+ > 40$). As the wall is approached, $\overline{\epsilon_2}$ is a much closer approximation to $\bar{\epsilon}$ than $\overline{\epsilon_1}$. Note that $\overline{\epsilon_2}$ overestimates $\bar{\epsilon}$ in the near-wall region whereas $\overline{\epsilon_1}$ underestimates it. As $x_2^+ \to 0$, $\overline{\epsilon_1}$ tends to zero while $\overline{\epsilon_2}$ tends to $2\nu\overline{u_{1,2}^2}$. At the wall, $\bar{\epsilon}$ is equal to $\nu(\overline{u_{1,2}^2} + \overline{u_{3,2}^2})$ which is significantly smaller than $2\nu\overline{u_{1,2}^2}$ since $\overline{u_{3,2}^2}$ is approximately $\frac{1}{4}\overline{u_{1,2}^2}$ near the wall (figure 4*a*).

The agreement of $\overline{\epsilon_1}$, and especially with $\overline{\epsilon_2}$, with $\bar{\epsilon}$ outside the buffer region has implications for the measurement of the dissipation in this part of the flow. All the terms in (19) can be obtained with a $1\frac{1}{2}$ ×-probe as used in I and Hussein (1988). The probe consists of three inclined wires, the central one being nominally at 45° to the flow, the other two being parallel at 135°. The configuration essentially replaces two laterally adjacent ×-wires but has the advantage of allowing the lateral separation (Δx_3 if the wires are in the (x_1, x_2)-plane; Δx_2 if they are in the (x_1, x_3)-plane) to be small without the possibility of increased flow interference from the supports of two

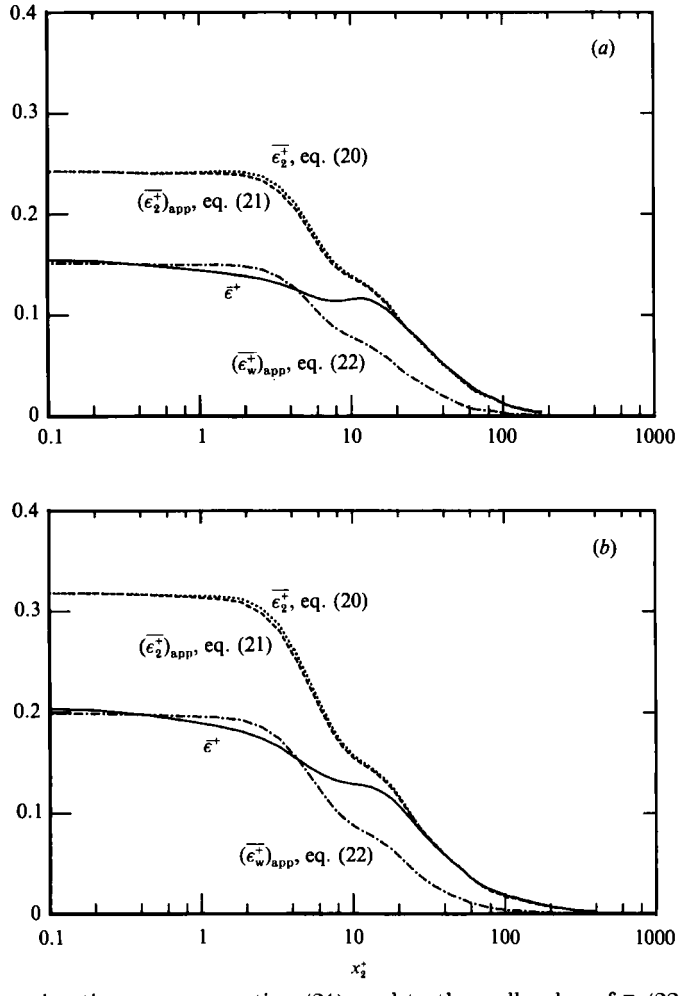

FIGURE 13. Approximations to $\overline{\epsilon_2}$, equation (21), and to the wall value of $\bar{\epsilon}$, (22). The distribution of $\bar{\epsilon}$ is also shown. (*a*) $h^+ = 180$; (*b*) $h^+ = 395$.

×-probes. Expression (20), which is more attractive experimentally than (19), contains $u_{1,2}$, a term which can be measured with parallel single hot wires. Measurements of $\theta_{,2}$ were made by Krishnamoorthy & Antonia (1987) in the wall region of a slightly heated boundary layer using parallel cold wires (diameter = 0.63 μm). Identical wires can be used for $u_{1,2}$ (the near-wall vicinity problem appears to mainly affect the measurement of $\bar{U}$, the fluctuating quantities being on the whole unaffected). However, the term $u_{2,2}$ is relatively difficult to measure, as it would involve the use of two ×-probes separated in the y-direction. Apart from the obviously stringent constraints on spatial resolution, it would be best to avoid measuring u_2 altogether (our experience and the literature suggest that the accurate measurement of this quantity with ×-wires is difficult, especially in the wall region). Figure 4(*b*, *c*) indicates that $\overline{u_{2,2}^2}$ is only slightly bigger than $\overline{u_{1,1}^2}$ and $\overline{u_{2,1}^2}$ is only slightly smaller than $\overline{u_{1,1}^2}$. Equation (20) was therefore reduced by trial to

$$(\overline{\epsilon_2})_{app} = \nu(2\overline{u_{1,2}^2} + 11\overline{u_{1,1}^2}). \tag{21}$$

This is a very close approximation to $\overline{\epsilon_2}$ (figure 13) and a good approximation to $\bar{\epsilon}$ for $x_2^+ \geqslant 30$.

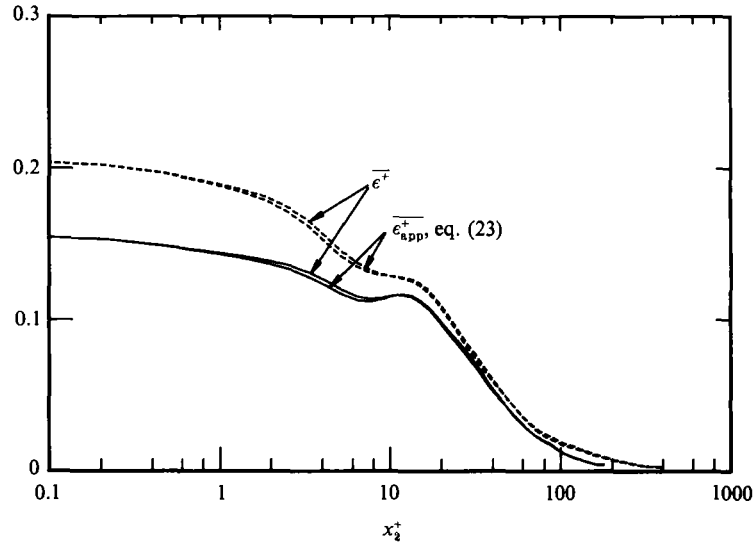

FIGURE 14. Approximation to $\bar{\epsilon}$, equation (23). ——, $h^+ = 180$; – – –, $h^+ = 395$.

Near the wall, axisymmetry is less relevant (as indicated by the AIMs in figure 7). The dominant terms in this region are $\overline{u_{1,2}^2}$ and $\overline{u_{3,2}^2}$. Since the latter term is equal to about $\frac{1}{4}\overline{u_{1,2}^2}$ (at both values of h^+), a reasonable approximation to the wall value of $\bar{\epsilon}$ should be

$$(\overline{\epsilon_w})_{app} \approx \nu(\tfrac{5}{4}\overline{u_{1,2}^2}). \tag{22}$$

This quantity, also shown in figure 13, provides a reasonable approximation for $\bar{\epsilon}$ in the sublayer but not in the buffer region. From a measurement viewpoint, (21) and (22) suggest that reasonable estimates of $\bar{\epsilon}$ can be obtained in the region $x_2^+ \geqslant 30$ and within the sublayer by using a pair of parallel hot wires (aligned in the x_3 direction). This should be quite a viable approach for $x_2^+ \geqslant 30$. It would be more difficult to implement within the sublayer, unless a relatively thick sublayer were available (e.g. the experiment of Eckelmann 1974 in a similar flow).

An expression which mimics $\bar{\epsilon}$ accurately everywhere in the flow should at least contain the three terms in figure 4(*a*) as they are important in the wall region. All the other terms in figure 4 are (individually) smaller in magnitude and have approximately the same shape. It was assumed that their sum could be approximated by $\alpha\overline{u_{1,1}^2}$ where the magnitude of α could be estimated by trial. It was found that $\alpha = 8$, namely

$$(\bar{\epsilon})_{app} = \nu(\overline{u_{1,2}^2} + \overline{u_{3,2}^2} + \overline{u_{1,3}^2} + 8\overline{u_{1,1}^2}) \tag{23}$$

provides a very close approximation of $\bar{\epsilon}$ everywhere in the flow (figure 14), the error being only 10% at $x_2^+ = 10$. All the terms in (23) can be measured with the $1\frac{1}{2}$ ×-probe. However, if it is difficult to get closer to the wall than $x_2^+ = 30$ with such a probe, approximation (21) can be more easily implemented (using a pair of parallel hot wires) than approximation (23).

It seems appropriate here to comment on the choice of the x_1 axis as the preferred direction in deriving the relations for local axisymmetry. It was noted in I that the choice of the mean flow direction is not unreasonable in the sense that, for most simple shear flows, $\overline{u_2^2} \approx \overline{u_3^2}$ (the transport equations for the normal stresses indicate that the energy is first supplied to $\overline{u_1^2}$ before it is distributed to the other components).

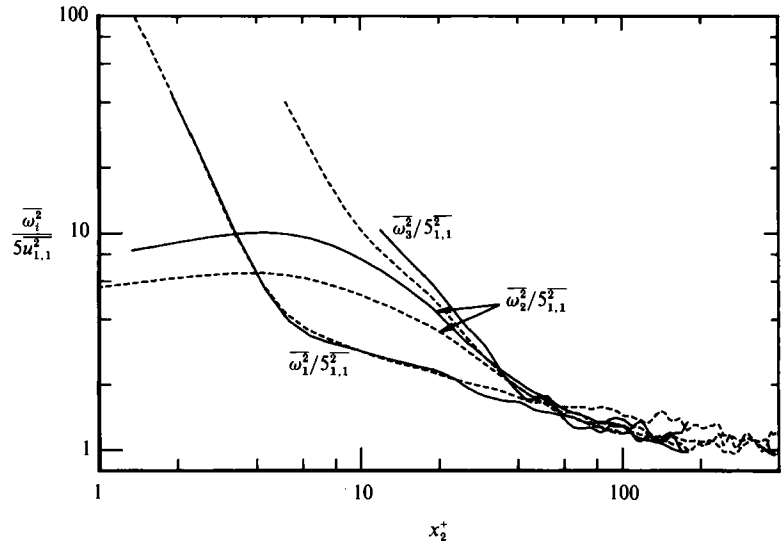

FIGURE 15. Comparison with isotropy of mean-square vorticity components. ——, $h^+ = 180$; – – –, $h^+ = 395$.

This symmetry is apparently reflected in the relations between mean-square velocity derivatives, as shown in (15) and figure 10. Although the results of I and the present ones represent adequate (*a posteriori*) justification for the use of x_1 as the preferred direction, it is nevertheless possible that there may be more appropriate choices for the preferred direction. One possibility, mentioned in I, is the direction (45°) of the principal axis of the local mean strain rate. This may, however, be quite different to the principal directions of the stress, dissipation or vorticity tensors. For example, the present data indicate that the principal stress is practically in the x_1 direction in the sublayer. As y^+ increases, the inclination increases to a maximum of about 20° (at $y^+ \approx 100$) before returning to 0° at the centre of the channel. It is finally worth noting that the information in figure 7 is, by definition of the AIM, independent of the choice of coordinate axes so that the comparison of the data with axisymmetry (figures 7 and 8) is also unaffected by this choice.

6. Implications for vorticity

Local axisymmetry (and local isotropy) requires that

$$\overline{\omega_2^2} = \overline{\omega_3^2}. \tag{24}$$

This follows from (10), (11), the first two relations in (15) and (16). Figure 15 shows that (24) is reasonably well approximated for $x_2^+ \geqslant 30$. (When $x_2^+ \geqslant 60$, $\overline{\omega_1^2}$ is also nearly equal to $\overline{\omega_2^2}$ or $\overline{\omega_3^2}$.) The isotropic values $\overline{\omega_1^2}, \overline{\omega_2^2}, \overline{\omega_3^2}$ are given by

$$\overline{\omega_1^2} = \overline{\omega_2^2} = \overline{\omega_3^2} = 5\overline{u_{1,1}^2}.$$

Figures 5 and 15 show that this is not valid except perhaps near the duct centreline.

Axisymmetric and isotropic expressions for $\overline{\omega_1^2}$ are different owing to the difference between (17) and (18). Substitution (17) into (9) results in a partially axisymmetric expression for $\overline{\omega_1^2}$, namely

$$\overline{\omega_1^2} = \overline{u_{3,2}^2} + \tfrac{5}{3}\overline{u_{2,3}^2} - \tfrac{1}{3}\overline{u_{1,1}^2}. \tag{25}$$

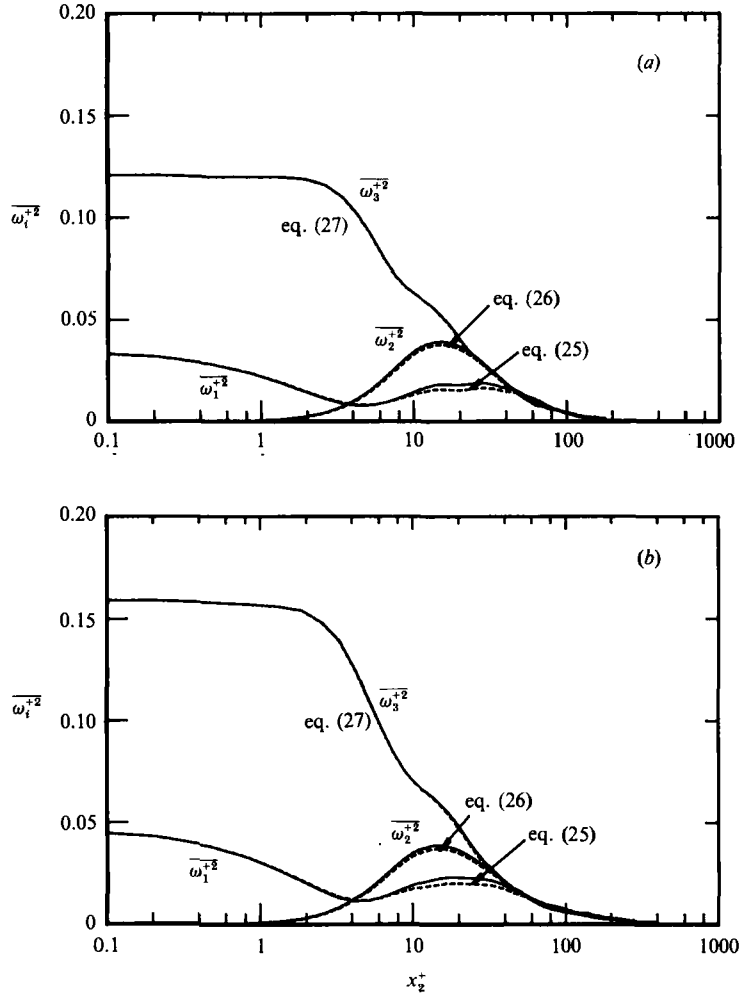

FIGURE 16. Approximations to $\overline{\omega_1^2}$, $\overline{\omega_2^2}$ and $\overline{\omega_3^2}$: $\overline{\omega_1^2}$, equation (25); $\overline{\omega_2^2}$, (26); $\overline{\omega_3^2}$, (27). (*a*) $h^+ = 180$; (*b*) $h^+ = 395$.

Axisymmetry would also require that $\overline{u_{3,2}^2}$ is equal to $\overline{u_{2,3}^2}$ (i.e. $M_4 = 1$, equation (15)) but this is only satisfied for $x_2^+ \geqslant 60$ (figure 10). As shown in figure 16, (25) is a good approximation to $\overline{\omega_1^2}$ almost everywhere (it underestimates slightly the local maximum of $\overline{\omega_1^{+2}}$ at $x_2^+ \approx 20$.

To provide approximations to $\overline{\omega_2^2}$ and $\overline{\omega_3^2}$, the major terms on the right-hand sides of (10) and (11) were retained and the others replaced by $\beta\overline{u_{1,1}^2}$. The following approximations (with $\beta = 2$):

$$\overline{\omega_2^2} = \overline{u_{1,3}^2} + 2\overline{u_{1,1}^2}, \tag{26}$$

$$\overline{\omega_3^2} = \overline{u_{1,2}^2} + 2\overline{u_{1,1}^2}, \tag{27}$$

are quite satisfactory (figure 16) for both values of h^+. A parallel-wire probe should allow relatively accurate measurements of $\overline{\omega_2^2}$ and $\overline{\omega_3^2}$ if use were made of (26) and (27). A $1\frac{1}{2}$ ×-probe should provide the data required to obtain $\overline{\omega_1^2}$ ($\overline{u_{3,2}^2}$ and $\overline{u_{2,3}^2}$ are obtained in separate experiments after a 90° rotation of the probe). Well-known difficulties of measuring x_2 and x_3 derivatives with hot wires are the selection of an

appropriate separation between the wires and a suitable method for correcting for the effect of this finite separation. The DNS database should be extremely valuable for selecting this separation and assessing the validity of the correction. For this reason, it is important that measurements be made in the same flow and Reynolds numbers as the present database, and such measurements are currently being planned. (It is also possible to check the effect of separation by directly assessing a model for a parallel-wire probe using a DNS database, in a manner similar to that used by Moin & Spalart (1989) in evaluating the response of an $\times$-probe.)

7. Conclusions

Direct numerical simulations of a fully developed turbulent channel flow at two low Reynolds numbers show that the mean-square values of the velocity derivatives, when normalized by wall variables, increase significantly with Reynolds number, particularly in the wall region (less than about 40 wall units). Consequently, the averaged dissipation and vorticity components are affected in a similar manner.

The average dissipation and mean-square vorticity are not consistent with local isotropy, except near the channel centreline. The assumption of axisymmetry, which is intermediate between the assumptions of homogeneity and local isotropy, allows reasonable estimates of $\overline{\epsilon}$ and $\overline{\omega^2}$ to be made outside the wall region. This assumption, which represents a relation of isotropy, makes it possible, therefore, to measure $\overline{\epsilon}$ and $\overline{\omega^2}$ outside the wall region using relatively simple hot-wire configurations. It has also been shown that $\overline{\epsilon}$ and the components of $\overline{\omega^2}$ can be closely approximated by expressions which should permit adequate measurements to be made everywhere in the flow.

Anisotropy invariant maps for the Reynolds stresses, dissipation and vorticity indicate that the degree of departure from axisymmetry does not seem to vary with Reynolds number. This is not altogether surprising since the present data and the available experimental evidence (e.g. Antonia *et al.* 1986) suggest that the deviation from local isotropy of mean-square values of velocity derivatives also appears to be independent of the Reynolds number.

The anisotropy invariant map for vorticity suggests a transition from a rod-like vortical structure very near the wall to a disk-like structure further away from the wall.

R.A.A. and L.W.B.B. acknowledge the support of the Australian Research Council and the Center for Turbulence Research.

REFERENCES

Antonia, R. A., Anselmet, F. & Chambers, A. J. 1986 Assessment of local isotropy using measurements in a turbulent plane jet. *J. Fluid Mech.* **163**, 365–391.

Antonia, R. A. & Bisset, D. K. 1990 Spanwise structure in the near-wall region of a turbulent boundary layer. *J. Fluid Mech.* **210**, 437–458.

Antonia, R. A., Browne, L. W. B. & Shah, D. A. 1988 Characteristics of vorticity fluctuations in a turbulent wake. *J. Fluid Mech.* **189**, 349–365.

Antonia, R. A., Krishnamoorthy, L. V. & Fulachier, L. 1988 Correlation between the longitudinal velocity fluctuation and temperature fluctuation in the near-wall region of a turbulent boundary layer. *Intl J. Heat Mass Transfer* **31**, 723–730.

Antonia, R. A., Shah, D. A. & Browne, L. W. B. 1987 Spectra of velocity derivatives in a turbulent wake. *Phys. Fluids* **30**, 3455–3462.

ANTONIA, R. A., TEITEL, M., KIM, J. & BROWNE, L. W. B. 1991 Low Reynolds number effects in a fully developed turbulent duct flow. *J. Fluid Mech.* (submitted).

BALINT, J.-L., VUKOSLAVČEVIĆ, P. & WALLACE, J. M. 1990 The transport of enstrophy in a turbulent boundary layer. In *Near-Wall Turbulence* (ed. S. J. Kline & N. H. Afgan), pp. 932–950. Hemisphere.

BATCHELOR, G. K. 1946 The theory of axisymmetric turbulence. *Proc. R. Soc. Lond.* A **186**, 480–502.

BATCHELOR, G. K. 1953 *The Theory of Homogeneous Turbulence.* Cambridge University Press.

BLACKWELDER, R. F. & SWEARINGEN, J. D. 1990 The role of inflectional velocity profiles in wall bounded flows. In *Near-Wall Turbulence* (ed. S. J. Kline & N. H. Afgan), pp. 268–288. New York, Hemisphere.

BROWNE, L. W. B., ANTONIA, R. A. & SHAH, D. A. 1987 Turbulent energy dissipation in a wake. *J. Fluid Mech.* **179**, 307–326.

CHAMPAGNE, F. H. 1978 The fine-scale structure of the turbulent velocity field. *J. Fluid Mech.* **86**, 67–108.

CHANDRASEKHAR, S. 1950 The theory of axisymmetric turbulence. *Proc. R. Soc. Lond.* A **242**, 557–577.

DEKEYSER, I., FULACHIER, L. & VEROLLET, E. 1977 Anisotropie du champ turbulent d'une couche limite. Influence de l'aspiration à la paroi. *J. Méc.* **16**, 605–623.

DRACOS, T., KHOLMYANSKY, M., KIT, E. & TSINOBER, A. 1990 Some experimental results on velocity–velocity gradient measurements in turbulent grid flows. In *Topological Fluid Mechanics* (ed. K. H. Moffatt & A. Tsinober). Cambridge University Press.

ECKELMANN, H. 1974 The structure of the viscous sublayer and the adjacent wall region in a turbulent channel flow. *J. Fluid Mech.* **65**, 439–459.

FOSS, J. F. & WALLACE, J. M. 1990 The measurement of vorticity in transitional and fully developed turbulent flows. In *Advances in Fluid Mechanics Measurements* (ed. M. Gad-el-Hak), vol. 45, pp. 263–322. Springer.

GEORGE, W. K. & HUSSEIN, H. J. 1991 Locally axisymmetric turbulence. *J. Fluid Mech.* **233**, 1–23 (referred to herein as I).

HUSSEIN, H. J. 1988 Measurements of small scale turbulence in an axisymmetric jet using moving hot wires. Ph.D. thesis, State University of New York at Buffalo.

KIM, J. 1989 On the structure of pressure fluctuations in simulated turbulent channel flow. *J. Fluid Mech.* **205**, 421–451.

KIM, J. & MOIN, P. 1989 Transport of passive scalars in a turbulent channel flow. In *Turbulent Shear Flows 6* (ed. J.-C. André, J. Constieux, F. Durst, B. Launder, F. Schmidt & J. Whitelaw), pp. 85–96. Springer.

KIM, J., MOIN, P. & MOSER, R. 1987 Turbulence statistics in fully developed channel flow at low Reynolds number. *J. Fluid Mech.* **177**, 133–166.

KRISHNAMOORTHY, L. V. & ANTONIA, R. A. 1987 Temperature dissipation measurements in a turbulent boundary layer. *J. Fluid Mech.* **176**, 265–281.

KUO, A. Y.-S. & CORRSIN, S. 1972 Experiment on the geometry of the fine-structure regions in fully turbulent fluid. *J. Fluid Mech.* **56**, 447–479.

LEE, M. J. & REYNOLDS, W. C. 1985 Numerical experiments on the structure of homogeneous turbulence. *Rep.* TF-24. Thermosciences Division, Stanford University.

LUMLEY, J. L. & NEWMAN, G. R. 1977 The return to isotropy of homogeneous turbulence. *J. Fluid Mech.* **82**, 161–178.

MANSOUR, N. N., KIM, J. & MOIN, P. 1988 Reynolds-stress and dissipation-rate budgets in a turbulent channel flow. *J. Fluid Mech.* **194**, 15–44.

MANSOUR, N. N., KIM, J. & MOIN, P. 1989 Near-Wall $k-\epsilon$ turbulence modeling. *AIAA J.* **27**, 1068–1073.

MOIN, P. & SPALART, P. R. 1989 Contributions of numerical simulation data bases to the physics, modeling and measurements of turbulence. In *Advances in Turbulence* (ed. W. K. George & R. Arndt), pp. 11–38. Hemisphere.

REYNOLDS, W. C. 1989 Effects of rotation on homogeneous turbulence. *Proc. Tenth Australasian Fluid Mechanics Conf.* (ed. A. E. Perry), KS2.1–KS2.6, University of Melbourne.

SPALART, P. R. 1988 Direct simulation of a turbulent boundary layer up to $R_\theta = 1410$. *J. Fluid Mech.* **187**, 61–98.

TAYLOR, G. I. 1935 Statistical theory of turbulence. *Proc. R. Soc. Lond.* A **151**, 421–478.

TOWNSEND, A. A. 1951 On the fine-scale structure of turbulence. *Proc. R. Soc. Lond.* A **28**, 534–542.